Available online at www.sciencedirect.com
SCIENCE DIRECT®
Journal of Computational Physics 194 (2004) 78–91
JOURNAL OF COMPUTATIONAL PHYSICS
www.elsevier.com/locate/jcp

Efficient numerical method for simulating static and dynamic properties of superfluid helium

L. Lehtovaara, T. Kiljunen [1], J. Eloranta *

Department of chemistry, University of Jyväskylä, Survontie 9, Jyväskylä 40500, Finland

Received 20 May 2003; received in revised form 25 August 2003; accepted 27 August 2003

Abstract

Density functional theory (DFT) offers computationally affordable way of describing static and dynamic properties of superfluid ^{4}He. In general, the DFT models yield single particle-like Schrödinger equations with a nonlinear potential term that accounts for all the many-body interactions. The resulting equations can be solved for small amplitude plane wave excitations in the bulk whereas fully numerical solution must be sought in more complicated cases. In this paper we propose a numerical method that can be used in solving the time-dependent nonlinear Schrödinger equation in both real and imaginary times. The method is based on operator splitting technique where each component operator is treated with a unitary semi-implicit Crank–Nicolson scheme. In order to increase the stability of the method for complex valued nonlinear potentials, a predict–correct scheme is employed in the simulations. The numerical calculations indicate that the scheme is numerically sufficiently stable and well behaving, exhibits high degree of parallelism, and produces results in agreement with the existing numerical data. In the numerical examples we apply the method to obtain dispersion relation of the bulk liquid and to calculate solvation and absorption spectrum of atomic boron solvated in superfluid helium.

Keywords: Density functional theory; Nonlinear Schrödinger equation; Semi-implicit; Crank–Nicolson; Predict–correct scheme

1. Introduction

Superfluid ^{4}He at 0 K constitutes a high-dimensional quantum system that follows Bose statistics. The large zero-point amplitude of the atoms efficiently overcomes the weak He–He binding and therefore the system behaves purely quantum mechanically. Elementary excitations of the bulk liquid are known by both experiments [1–3] and theory [4], although in the latter case the analytic treatments can only be carried out approximately. The neutron scattering experiments gave the form for very unusual dispersion relation, which has both positive and negative slopes. Approximate analytic treatment of Feynman and Cohen [4]

* Corresponding author. Tel.: +358-050-373-2122; fax: +358-014-260-2551.
E-mail address: eloranta@jyu.fi (J. Eloranta).
[1] Present address: Institut für Experimentalphysik, Freie Universität Berlin, Arnimallee 14, Berlin 14195, Germany.

0021-9991/$ - see front matter
doi:10.1016/j.jcp.2003.08.020

was able to reproduce the shape of the dispersion curve and rationalize the nature of excitations (i.e., phonons and rotons). When the liquid density profiles differ significantly from the constant bulk behavior, the situation becomes more complicated and most often numerical calculations are the only way to proceed. Two separate branches of methods have been developed to solve the high dimensional quantum problem: quantum Monte Carlo (QMC) and density functional theory (DFT). QMC aims at direct random sampling of the high dimensional n-particle space and most of its variants are asymptotically exact with respect to simulation time. Some QMC methods have also been extended to describe excited states and therefore it can also describe liquid at finite temperatures. The main drawback of the QMC is that it can only yield stationary solutions with respect to time or at most dynamics in imaginary time. Another approach based on DFT relies on existence of a dimension reduction operation that maps the n-particle problem into effective single particle-like problem. The main disadvantage is that the form of this mapping is not known and one must resort to calibration against experimental data in order to find a good approximation for it. The first such mapping was given by the Gross–Pitaevskii (GP) theory [5–7], which has been extensively used in describing superfluid helium. However, at its best this theory can describe only the initial phonon branch of the liquid dispersion relation and therefore it has no knowledge of peculiarities of the superfluid helium, like the roton branch. Historically the GP theory points an important relation of the DFT models to the classical fluid dynamics via the Madelung transformation [8]. This allows, for example, use of fluid dynamical concepts in developing new functionals. Since the GP theory there has been significant advances in developing new functionals, which can now reproduce many experimental observables of the bulk superfluid liquid. These properties include bulk dispersion relation, pressure dependency of sound velocity, and liquid compressibility. Although the present paper concentrates on the works of Dupont-Roc et al. [9] and Stringari et al. [10], we also note that functionals with similar capabilities have been proposed, for example, by Berloff [11]. In addition to describing bulk properties, these functionals have also been shown to be able to model inhomogeneous liquid density profiles [12]. In contrast to QMC the DFT allows time-dependent formulation and can therefore conveniently be applied in describing superfluid dynamics at 0 K [13]. Furthermore, combined DFT and thermodynamic models have been developed that can provide proper statistical picture of the thermal excitations [14] and thus extend the model to finite temperature case.

Experiments carried out by physics and chemical physics communities have provided wealth of experimental data regarding static and dynamic solvation of impurities in liquid helium. Examples of such impurities are electrons [15–18] and various atoms and diatomic excimers [19–22]. The static solvation structures surrounding the impurity can be classified as bubbles or snowballs depending on properties of the impurity–He pair potential. The degree of liquid inhomogeneity depends naturally on the selected impurity center and can range from almost a free surface to solid layers of helium. The present functionals have shown excellent agreement with the known QMC and experimental data in the weakly inhomogeneous cases [10]. On the other hand in strongly inhomogeneous cases serious convergence problems of even the most advanced DFT models have been observed [23]. In such cases hybrid QMC/DFT methods have proven useful provided that a suitable dividing layer between the molecular complex and the liquid exists [23]. However, much less is known about the cases where the impurity–He pair potential is anisotropic as the high symmetry for the liquid is lost [12,23]. With respect to superfluid dynamics that considers liquid flow, very few applications of DFT have been published, as the related experimental data is scarce [13,24]. Mainly two types of time resolved experiments have been carried out: measurement of drift velocities of charged species [25] and pump–probe measurement of the quantum bath dynamics [26]. The first case has been modeled, for example, by Berloff, where the electron drift and critical velocity phenomena were evaluated by DFT [27]. In the latter case, the DFT calculations have been able to provide correct time scales for the quantum bath dynamics [13,26].

It is clear from the above considerations that many systems include anisotropic interactions and therefore it is of interest to develop a numerical DFT method that can describe the liquid in full 3-D using

both time-independent and time-dependent formalisms. In these calculations computer execution time and memory storage space become a major concern. From the numerical point of view we will utilize the following methodologies: Fourier transform based evaluation of the nonlinear DFT potential and semi-implicit Crank–Nicolson scheme in the position representation. The stability and parallel execution efficiency of the method are demonstrated by using numerical simulations. These simulations include examples of static solvation of atomic boron in superfluid helium, calculation of its optical 3s ← 2p transition in liquid, and evaluation of the bulk liquid dispersion relation.

2. Density functional model

Liquid ^{4}He can be described using DFT, by reducing the many-body problem to an effective single particle Schrödinger-like equation. The energy functional of Dupont–Roc et al. (DR), not including any impurity–liquid interaction, is defined as follows [9]:

$$E_{\mathrm{DR}}[\Psi] = \frac{\hbar^2}{2M_{\mathrm{He}}}\int |\nabla\Psi(r)|^2\,\mathrm{d}^3r + \frac{1}{2}\int\int \rho(r)U_l(|r-r'|)\rho(r')\,\mathrm{d}^3r'\,\mathrm{d}^3r + \frac{c}{2}\int \rho(r)(\overline{\rho}(r))^{1+\gamma}\,\mathrm{d}^3r, \tag{1}$$

where $\rho(r) = |\Psi(r)|^2$ and the auxiliary functions are defined as:

$$\begin{aligned} U_l(r) &= \begin{cases} 4\varepsilon\left[\left(\frac{\sigma}{r}\right)^{12} - \left(\frac{\sigma}{r}\right)^{6}\right], & \text{when } r \geqslant h, \\ U_l(h)\left(\frac{r}{h}\right)^4, & \text{when } r < h, \end{cases} \\ \overline{\rho}(r) &= \int \rho(r')\Pi_h(|r-r'|)\,\mathrm{d}^3r', \quad \text{where } \Pi_h(r) = \begin{cases} \frac{3}{4\pi h^3}, & \text{when } r \leqslant h, \\ 0, & \text{when } r > h, \end{cases} \end{aligned} \tag{2}$$

where the screening distance h is 2.377 Å and model parameters c and γ are 10,455,400 K Å$^{3+3\gamma}$ and 2.8, respectively. The U_l function assumes a Lennard–Jones interaction at long range, with parameters $\epsilon = 10.22$ K and $\sigma = 2.556$ Å, and screening at short range. The auxiliary function in Eq. (2) provides spherical averaging for the liquid density. An extension of this functional has been proposed by Dalfovo, Stringari et al. (SD) as follows [10]:

$$\begin{aligned} E_{\mathrm{SD}}[\Psi] = {} & \frac{\hbar^2}{2M_{\mathrm{He}}}\int |\nabla\Psi(r)|^2\,\mathrm{d}^3r + \frac{1}{2}\int\int \rho(r)U_l^e(|r-r'|)\rho(r')\,\mathrm{d}^3r'\,\mathrm{d}^3r \\ & + \frac{c_2}{2}\int \rho(r)(\overline{\rho}(r))^2\,\mathrm{d}^3r + \frac{c_3}{3}\int \rho(r)(\overline{\rho}(r))^3\,\mathrm{d}^3r \\ & - \frac{\hbar^2\alpha_s}{4M_{\mathrm{He}}}\int\int F(|r-r'|)\left(1-\frac{\tilde{\rho}(r)}{\rho_{0s}}\right)\nabla\rho(r)\cdot\nabla\rho(r')\left(1-\frac{\tilde{\rho}(r')}{\rho_{0s}}\right)\mathrm{d}^3r'\,\mathrm{d}^3r, \end{aligned} \tag{3}$$

where U_l^e corresponds to the Lennard–Jones pair potential ($\sigma = 2.556$ Å and $\varepsilon = 10.22$ K) with complete screening at short distances ($U_l^e \equiv 0$ when $|r-r'| \leqslant h, h = 2.1903$ Å), $c_2 = -2.411857 \times 10^4$ K Å^6, $c_3 = 1.858496 \times 10^6$ K Å^9, $\alpha_s = 54.31$ Å^3, $\rho_{0s} = 0.04$ Å^{-3}, and $F(r)$ is defined as Gaussian ($F(r) = \pi^{-3/2}l^{-3}\exp(-r^2/l^2)$ with $l = 1$ Å). $\tilde{\rho}$ is defined as convolution of the density ρ with function F. This functional has been applied, for example, to describe the static properties of He_2^* excimer bubbles in superfluid helium [12]. Improved behavior in dynamical applications can be expected from the functional of Dalfovo et al. [10] (e.g., Eqs. (3) and (4)), which accounts for backflow (SD–BF):

$$E_{\mathrm{BF}}[\Psi(r,t)] = -\frac{M_{\mathrm{He}}}{4}\int\int U_j(|r-r'|)\rho(r,t)\rho(r',t)(v(r,t)-v(r',t))^2\,\mathrm{d}^3r'\,\mathrm{d}^3r, \tag{4}$$

where velocity is defined through the probability current

$$v(r) = -\frac{\mathrm{i}\hbar}{2M_{\mathrm{He}}}\left(\frac{\nabla\psi(r)}{\psi(r)} - \frac{\nabla\psi^*(r)}{\psi^*(r)}\right), \tag{5}$$

and U_j is expressed as

$$U_j(r) = (\gamma_{11}+\gamma_{12}r^2)\,\mathrm{e}^{-\alpha_1 r^2} + (\gamma_{21}+\gamma_{22}r^2)\,\mathrm{e}^{-\alpha_2 r^2} \tag{6}$$

and $\gamma_{11} = -19.7544$, $\gamma_{21} = -0.2395$, $\gamma_{12} = 12.5616$ Å^{-2}, $\gamma_{22} = 0.0312$ Å^{-2}, $\alpha_1 = 1.023$ Å^{-2}, and $\alpha_2 = 0.14912$ Å^{-2}. The following DFT calculations require functional derivatives for Eqs. (1), (3), and (4). For the first energy expression, we get

$$\begin{aligned}\frac{\delta E_{\mathrm{DR}}}{\delta\psi^*} = & -\frac{\hbar^2}{2M_{\mathrm{He}}}\Delta\psi(r) + \int \rho(r')U_l(|r-r'|)\,\mathrm{d}^3r'\psi(r)\\ & + \frac{c}{2}(\bar\rho(r))^{1+\gamma}\psi(r) + \frac{c}{2}(1+\gamma)\int \Pi_h(|r-r'|)\rho(r')(\bar\rho(r'))^{\gamma}\,\mathrm{d}^3r'\psi(r).\end{aligned} \tag{7}$$

For Eq. (3), we get

$$\begin{aligned}\frac{\delta E_{\mathrm{SD}}}{\delta\psi^*} = & -\frac{\hbar^2}{2M_{\mathrm{He}}}\Delta\psi(r) + \int \rho(r')U_l^e(|r-r'|)\,\mathrm{d}^3r'\psi(r)\\ & + \frac{c_2}{2}(\bar\rho(r))^2\psi(r) + c_2\int \Pi_h(|r-r'|)\rho(r')\bar\rho(r')\,\mathrm{d}^3r'\psi(r)\\ & + \frac{c_3}{3}(\bar\rho(r))^3\psi(r) + c_3\int \Pi_h(|r-r'|)\rho(r')(\bar\rho(r'))^2\,\mathrm{d}^3r'\psi(r)\\ & + \frac{\hbar^2\alpha_s}{2M_{\mathrm{He}}}\Bigg\{\left(1-\frac{\tilde\rho(r)}{\rho_{0s}}\right)\int(\nabla_r F(|r-r_1|))\cdot\underbrace{(\nabla_{r_1}\rho(r_1))\left(1-\frac{\tilde\rho(r_1)}{\rho_{0s}}\right)}_{\equiv G(r_1)}\,\mathrm{d}^3r_1\\ & + \int F(|r-r_1|)\overbrace{(\nabla_{r_1}\rho(r_1))\cdot\underbrace{\int F(|r_1-r_2|)\underbrace{(\nabla_{r_2}\rho(r_2))\left(1-\frac{\tilde\rho(r_2)}{\rho_{0s}}\right)}_{\equiv G(r_2)}\,\mathrm{d}^3r_2}_{\equiv J(r_1)}}^{\equiv H(r_1)}\,\mathrm{d}^3r_1\\ & - \underbrace{\int F(|r-r_1|)\underbrace{(\nabla_{r_1}\rho(r_1))\left(1-\frac{\tilde\rho(r_1)}{\rho_{0s}}\right)}_{\equiv G(r_1)}\,\mathrm{d}^3r_1}_{\equiv J(r)}\cdot\int(\nabla_r F(|r-r_2|))\rho(r_2)\,\mathrm{d}^3r_2\Bigg\}\psi(r),\end{aligned} \tag{8}$$

where the last two lines appear from the exact treatment of the non-local kinetic energy functional (compare, for example, to [12]). For Eq. (4) the functional derivative can be obtained as

$$\begin{aligned}\frac{\delta E_{\mathrm{BF}}}{\delta\psi^*} &= \left\{ -\frac{M_{\mathrm{He}}}{2}\int U_j(|r-r'|)\rho(r')(v(r)-v(r'))^2\,\mathrm{d}^3r' \right.\\ &\quad \left. +\frac{\mathrm{i}}{2\rho(r)}\nabla_R\cdot\int U_j(|r-r'|)\rho(r)\rho(r')(v(r)-v(r'))\,\mathrm{d}^3r'\right\}\psi(r)\\ &= \left\{ -\frac{M_{\mathrm{He}}}{2}[v(r)\cdot(v(r)A(r)-B(r))-v(r)\cdot B(r)+C(r)]\right.\\ &\quad \left. +\frac{\mathrm{i}}{2}\left[\left(\frac{\nabla\rho(r)}{\rho(r)}+\nabla\right)\cdot(v(r)A(r)-B(r))\right]\right\}\psi(r),\end{aligned}$$

where

$$\begin{aligned}A(r) &= \int U_j(|r-r'|)\rho(r')\,\mathrm{d}^3r',\\ B(r) &= \int U_j(|r-r'|)\rho(r')v(r')\,\mathrm{d}^3r',\\ C(r) &= \int U_j(|r-r'|)\rho(r')|v(r')|^2\,\mathrm{d}^3r'.\end{aligned} \tag{9}$$

This part of the effective potential has both real and imaginary terms, which act on both phase of the wavefunction as well as its local amplitude in such a way that the total integral norm of the wavefunction is conserved during time integration.

Stationary solutions (i.e., $\delta E/\delta\Psi^* = 0$) for energy functional can be obtained via the self-consistent treatment of the time-independent density functional equation:

$$\frac{\delta E}{\delta\psi^*}-\mu\Psi(r)\equiv-\frac{\hbar^2}{2M_{\mathrm{He}}}\Delta\Psi(r)+V[\rho(r)]\Psi(r)-\mu\Psi(r)=0, \tag{10}$$

where E is given energy functional (e.g., DR; Eq. (1) or SD; Eq. (3)), $V[\rho(r)]$ is the corresponding effective nonlinear potential that depends on liquid density $\rho=|\Psi|^2$, and μ is the chemical potential (average energy per boson; $\sim$−7 K/atom). Instead of directly solving Eq. (10), we use an alternative approach that is based on imaginary time propagation. This method is, for example, a key element in diffusion Monte Carlo. Thus both time-dependent and independent results can be obtained by solving the time-dependent DFT equation in real or imaginary time:

$$\mathrm{i}\hbar\frac{\partial\Psi(r,t)}{\partial t}=\frac{\delta E}{\delta\psi^*}-\mu\psi(r,t)=-\frac{\hbar^2}{2M_{\mathrm{He}}}\Delta\Psi(r,t)+V[\Psi(r,t)]\Psi(r,t)-\mu\Psi(r,t). \tag{11}$$

This equation results from the least action principle, which requires that $\Psi^*(r,t)$ is a stationary state solution with respect to variations $\delta\Psi^*(r,t)$. Subtraction of the chemical potential from the left side of Eq. (11) merely removes a constant phase factor from the wavefunction. Eq. (11) is subject to periodic spatial boundary conditions, which makes it compatible with the Fourier transform based evaluation of the effective potential. Finally, it should be noted that we are not implying any physical interpretation on the "wavefunction" Ψ. It merely arises from a Madelung-type change of variables from S and ρ in [10] to a complex valued Ψ. Furthermore, it should be noted that in [28] S is given a meaning of phase instead of a continuous variable, which allows description of quantitized vortices, for example.

3. Numerical method

In the following we present implementation for a true three-dimensional DFT-based numerical method that can describe both static and dynamic properties of superfluid ^{4}He. To begin with, Eq. (11) can be viewed in either momentum or position spaces. For the present implementation we have chosen the latter representation. Spatial discretization of the wavefunction is then carried out using a regular Cartesian rectangular grid in 3-D. In addition to its generality, it will allow efficient use of the fast Fourier transform (FFT) method for evaluation of the nonlinear effective potential V. For time integration of Eq. (11), we will apply the splitted operator scheme combined with a semi-implicit Crank–Nicolson method. The present potential evaluation and time propagation schemes will bring the computational cost from $\mathrm{O}(N^6)$ down to $\mathrm{O}(N^3 \log N)$, where N is the total number of grid points along each axis.

3.1. Evaluation of the nonlinear potential

Both Eqs. (7) and (8) contain convolution integrals between the liquid density and the screened Lennard–Jones potential. Since Eq. (11) is subject to periodic boundary conditions, it is natural to calculate the integrals by using the fact that a convolution reduces to a local multiplication operation in the Fourier space [29]. Thus calculation of such integral requires two forward FFTs and one backward FFT. As some of the functions in convolutions do not change during the simulation, they need to be transformed only once. Similar strategy can be used for the spherical average terms in Eqs. (7) and (8). The last three lines in Eq. (8) originate from the non-local kinetic energy correlation term of Eq. (3). This term has been written in such a from that the convolution theorem may be applied. Suitable choice of functions for convolution has been indicated in Eq. (8) by functions H and G. The backflow functional derivative (Eq. (9)) also clearly shows the proper convolution form. For efficient FFT library we have chosen the FFTW package, for which a good parallel implementation using threads (e.g., shared memory computer) is available [30]. In the present problem, the FFT step determines the overall computational cost of the method.

3.2. Time-space discretitzation of the DFT equations

The present DFT problem is essentially a time-dependent nonlinear Schrödinger equation of the form:

$$\mathrm{i}\hbar \frac{\partial \psi(r,t)}{\partial t} = H\psi(r,t), \tag{12}$$

where $H = T + V$ is the nonlinear DFT operator consisting of the kinetic and potential contributions (e.g., Eq. (11)). The formal solution for this equation can approximated by writing

$$\psi(r,t+\Delta t) \approx \exp\left\{ -(\mathrm{i}/\hbar) \int_t^{t+\Delta t} H[\psi(r,t')]\,\mathrm{d}t' \right\} \psi(r,t) \approx \exp\{ -(\mathrm{i}/\hbar) H[\psi(r,t)]\Delta t\}\psi(r,t). \tag{13}$$

The last equality holds exactly if the potential term of H is linear in ψ (e.g., time-independent). However, it is still a good approximation when H is only mildly nonlinear. For both DR and SD functionals this approximation works well whereas for SD–BF (cf. Eq. (4)) it fails due to instability produced by the imaginary component present in the backflow potential. Later in the text the method will be extended to reduce this instability. For now, we just directly apply the approximate propagator of Eq. (13). The potential energy operator V in H is taken to be diagonal even though, it strictly speaking, contains off diagonals as the gradients of wavefunctions occur in the kinetic energy correlation term. This is a good approximation since the main off diagonal contribution originates from the single particle kinetic energy. The Laplacian in the single particle kinetic energy operator was discretized using the standard three-point

finite difference stencil along each Cartesian axis. This gives second-order ($O(h^2)$) accurate approximation for the spatial degrees of freedom. An extensive review of the finite difference methods applied to the Schrödinger-type problems has been given in [31]. The total energy operator is splitted into components and written in symmetric form as follows (order of accuracy Δt^3):

$$\psi(r,t+\Delta t) \approx \exp\{-(\mathrm{i}/2)T_x\Delta t/\hbar\}\exp\{-(\mathrm{i}/2)T_y\Delta t/\hbar\}\exp\{-(\mathrm{i}/2)T_z\Delta t/\hbar\}\exp\{-\mathrm{i}V[\psi(r,t)]\Delta t/\hbar\} \times \exp\{-(\mathrm{i}/2)T_z\Delta t/\hbar\}\exp\{-(\mathrm{i}/2)T_y\Delta t/\hbar\}\exp\{-(\mathrm{i}/2)T_x\Delta t/\hbar\}\psi(r,t), \tag{14}$$

where T_x, T_y, and T_z are the Cartesian components of the kinetic energy and V is the nonlinear potential. In principle only Δt^2 accuracy is required for present purposes and therefore it is not necessary to use the symmetrized form in Eq. (14). For propagating each of the component operators (O) over time Δt we use the unitary Crank–Nicolson scheme (order of accuracy Δt^2) [29]:

$$\left(1+\frac{\mathrm{i}}{2\hbar}O\Delta t\right)\psi(r,t+\Delta t) = \left(1-\frac{\mathrm{i}}{2\hbar}O\Delta t\right)\psi(r,t). \tag{15}$$

Thus overall both space and time are treated to the same order of accuracy (i.e., Δx^2 and Δt^2). Propagation of each cartesian component of the kinetic energy leads to a set of linear equations corresponding to a cyclic tridiagonal matrix. Such equations can be solved efficiently by standard decomposition methods (e.g., Sherman–Morrison formula) [29]. In principle, the present problem could alternatively be formulated in the momentum space, which would effectively reduce one FFT from the computation. For DR and SD functionals the method allows sufficiently long time steps to be used, usually up to 80 fs. Parallelization of the time integration scheme was implemented using OpenMP directives [32] on shared memory computer (IBM pSeriers 690) using up to 32 processors.

As noted earlier, the backflow term of Eq. (4) is numerically unstable using the previously described method. In order to avoid the problem, we have implemented predictor–corrector-type scheme for the nonlinear potential of Eq. (14). For predicting step we use the previously described method with the potential evaluated at time t (e.g., $V[\psi(r,t)]$) and thus obtain an approximation for the nonlinear potential $V[\psi(r,t+\Delta t)]$ at $t+\Delta t$. The corrector step is then carried out using the same method but with the nonlinear potential being average of the present and predicted potentials, $V_{\mathrm{corr}} = (V[\psi(r,t)] + V[\psi(r,t+\Delta t)])/2$. This semi-implicit Crank–Nicolson method attempts to preserve the time reversal symmetry and makes the overall time integration method for the SD–BF functional numerically sufficiently stable. With this extension, time steps up to 80 fs can be used in the SD–BF simulations. Recently, we have learned that the present predict–correct approach is identical to the one that has been applied in solving the time-dependent electronic Kohn–Sham equations [33]. However, in that case, the nonlinear potential is purely real valued which makes the Kohn–Sham problem less demanding from the numerical point of view.

4. Numerical examples

In order to test the numerical method, we will concentrate on two test cases, which demonstrate both real and imaginary time propagation of the DFT equations for homogeneous and inhomogeneous liquids. First inhomogeneities are introduced by placing an atomic impurity, a boron atom in the present case, in bulk liquid. This choice was based on the following criteria: the boron–helium potential is relatively weakly bound (at most ~20 K), which is suitable for the present DFT models (see [23] for further discussion on this issue), the ground state boron–helium potential is anisotropic (cylindrical symmetry), and optical $3s \leftarrow 2p$ absorption spectrum can be calculated using the time-dependent perturbation theory. For homogeneous liquids we will concentrate on evaluation of the known dispersion relations, which will provide clear evidence for correctness of the present calculations.

4.1. Static solvation of boron atom in superfluid helium

The interaction between boron atom and bulk helium is given by the following convolution:

$$E_{\mathrm{IM}}[\psi] = \int U_{\mathrm{IM}}(|r - r'|)\rho(r')\,\mathrm{d}^3 r', \tag{16}$$

where U_{IM} is the pair potential between the boron atom and a single He (^{1}S) atom. This pair potential was obtained by ab initio coupled cluster with single, double, and perturbative triple substitutions (UCCSD(T)) method for the lowest $^2\Sigma$ and $^2\Pi$ states whereas multi-reference configuration interaction (MRCI) calculation was used in obtaining the excited $^2\Sigma$ state that correlates to excited atomic boron $1s^2 2s^2 3s^1$ configuration. In both calculations the augmented correlation consistent basis set aug-cc-pV5Z of Dunning et al. was used [34–36]. The electron structure calculations were carried out using the Molpro-program suite [37]. For detailed description of the methodology used in the present calculations, see [38,39]. Results from the calculations are shown in Fig. 1 where the three lowest states for B–He are plotted.

In the following we concentrate on imaginary time solution of Eqs. (3) and (8) (i.e., $t \to it$), where contribution from Eq. (16) has been added. Since these calculations seek for the ground state solution, the backflow energy of Eq. (9) will be zero. In each case the initial "wavefunction" was taken to correspond to constant liquid density ($\rho_0 = 0.0218360$ Å^{-3}). For the present case sufficient imaginary time step was found to be 10 fs. The atomic zero-point motion within the bubble as well as possible many-body effects in the B–He potential have been ignored in the present calculations. Furthermore, it has been assumed that the liquid will break the p-orbital frame degeneracy (e.g., crystal field splitting, see for example, [38]). This process is expected to take place by any asymmetric motion of the liquid (e.g., thermal excitations) and should therefore resemble situation encountered in the real experiments.

In Fig. 2 we show the calculated liquid ground state density around a ground state boron atom. As the potential U_{IM} has cylindrical symmetry, the obtained solution retains naturally the same symmetry. Due to binding ($\sim$20 K) in the diatomic $^2\Pi$ state, the liquid packs around the neck of the boron atomic p-orbital. In Fig. 3 the liquid density distribution around the electronically excited state boron atom (^{2}S) is shown

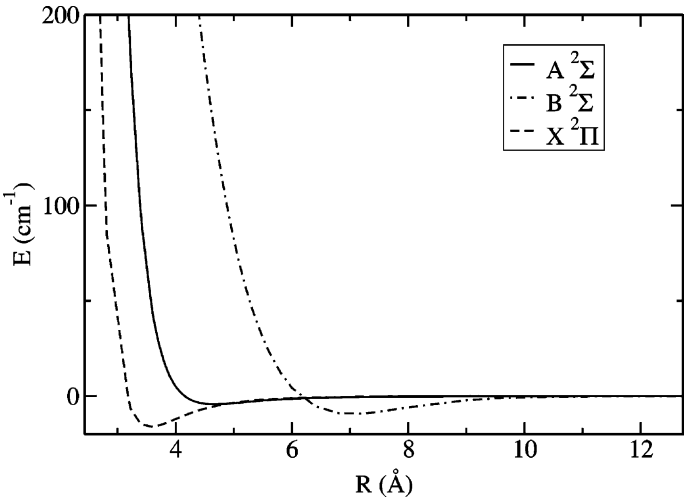

Fig. 1. Pair potentials of B–He interaction for the lowest $^2\Pi$ state (X) and the two lowest $^2\Sigma$ states (A,B) as obtained from the ab initio calculations are shown. All the atomic asympotes have been adjusted to zero. Two of the lowest states correlate to ground state boron atom whereas the second $^2\Sigma$ (B) state correlates to ^{2}S atomic asymptote.

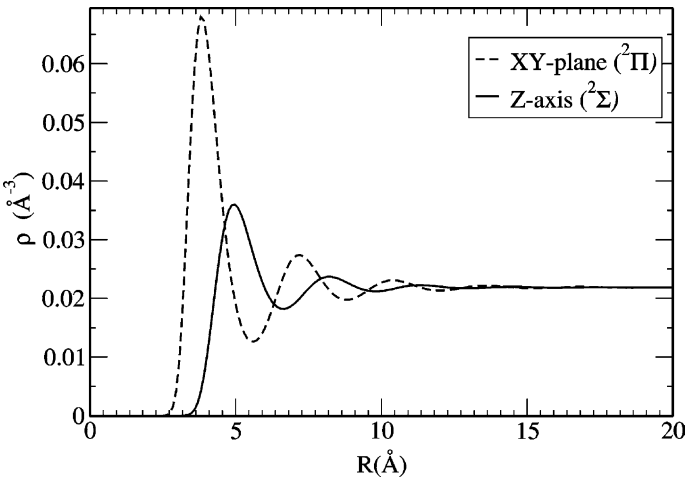

Fig. 2. Superfluid ground state density around boron atom is shown along both axial (XY) and longitudinal directions (Z). A spatial grid of $384 \times 384 \times 384$ with 0.1 Å step was applied in the calculation. Time integration was executed for 500 iterations with 10 fs time step.

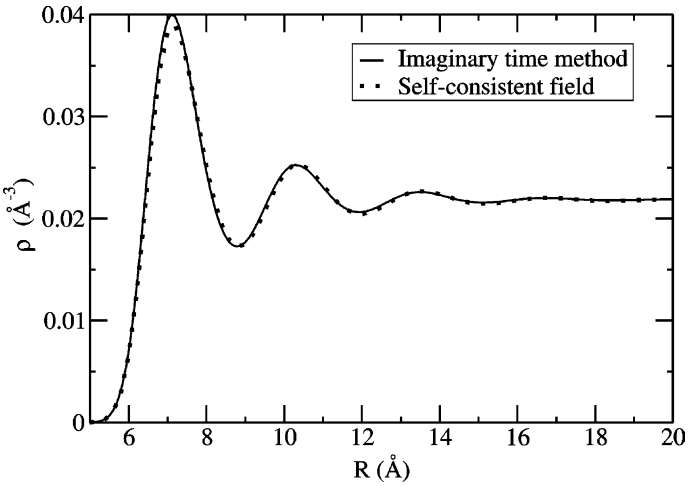

Fig. 3. Superfluid ground state density around electronically excited boron atom (^{2}S) is plotted. Overall the liquid retains spherical symmetry corresponding to the symmetry of the boron–He pair potential. Liquid density obtained from the 1-D self-consistent field method of Eloranta et al. [12] is also shown for reference. Parameters used in the calculation are identical to those in Fig. 2. The result was obtained after 200 simulation steps.

along with results obtained from the 1-D self-consistent field method of [12]. In this case the bubble formed in the liquid is spherically symmetric having approximate bubble radius of $\sim$6.5 Å.

Given the liquid ground state solution, it is now possible to calculate the atomic boron 3s $\leftarrow$ 2p optical absorption spectrum in liquid helium. A general recipe for calculating such spectrum $I(\omega)$ in condensed phase is based on the time-dependent perturbation theory [40,41]

$$I(\omega) \propto \int_{-\infty}^{\infty} \mathrm{e}^{\mathrm{i}\omega t} c(t)\,\mathrm{d}t, \tag{17}$$

where $c(t)$ is the time-correlation function, which is defined as:

$$c(t) = \left\langle \psi_{\mathrm{n}}^{(i)} \middle| \mathrm{e}^{\mathrm{i}H_{\mathrm{i}}t/\hbar}\hat{\mu}\,\mathrm{e}^{-\mathrm{i}H_{\mathrm{f}}t/\hbar}\hat{\mu} \middle| \psi_{\mathrm{n}}^{(i)} \right\rangle, \tag{18}$$

where ψ_{n} refers to nuclear wavefunctions, μ to the electronic dipole transition operator, and $H_{\mathrm{i,f}}$ to the nuclear Hamiltonians for the initial and the final states, respectively. Most of the spectral shifting and broadening is caused by the low density He gas close to the atomic impurity and therefore the time correlation function can be approximated using the Anderson's formula [42]:

$$c(t) = \exp\left[-\int (1 - \mathrm{e}^{-\mathrm{i}\Delta V_{\mathrm{fi}}(r)t/\hbar})\rho_i(r)\,\mathrm{d}^3 r \right], \tag{19}$$

where ΔV_{fi} is the difference potential between the ground electronic and excited states and ρ_i is the liquid density in the electronic ground state. This method avoids explicit consideration of both electron and nuclear dynamics in computation of $c(t)$. The calculated absorption spectrum is shown in Fig. 4. The spectrum is strongly blue shifted and broadened as compared to the gas phase because the ground and excited states have different symmetries.

4.2. Dispersion relations

By evaluating Eq. (11) in real time, it is possible to model dynamics in superfluid helium. A rigorous test is to reproduce the known bulk dispersion relations with small amplitude excitations for the functionals of Section 2. Such relation can be obtained conveniently by introducing a linear combination of plane waves along some given axis with given momenta (k_i) on top of the ground state wavefunction:

$$\psi(r,0) = \sqrt{\rho_0} + \sum_{i=1}^{N} a_i\,\mathrm{e}^{\mathrm{i}k_i x}, \quad \text{where } k_i = \frac{2\pi n_i}{L}, \tag{20}$$

where constants a_i were chosen to introduce small deviations from the ground state liquid (0.1% of bulk density), L is the length of the simulation cube side, and n_i are chosen to cover the desired range of

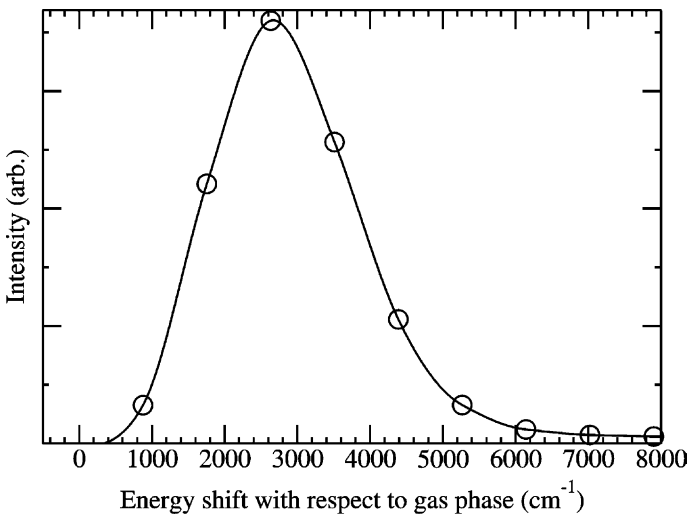

Fig. 4. Optical absorption spectrum of boron 3s ← 2p transition is shown. The spectrum was simulated using Eqs. (17)–(19). Line broadening is completely due to electronic dephasing. The gas phase electronic origin for the transition is at ca. 40032 cm^{-1}.

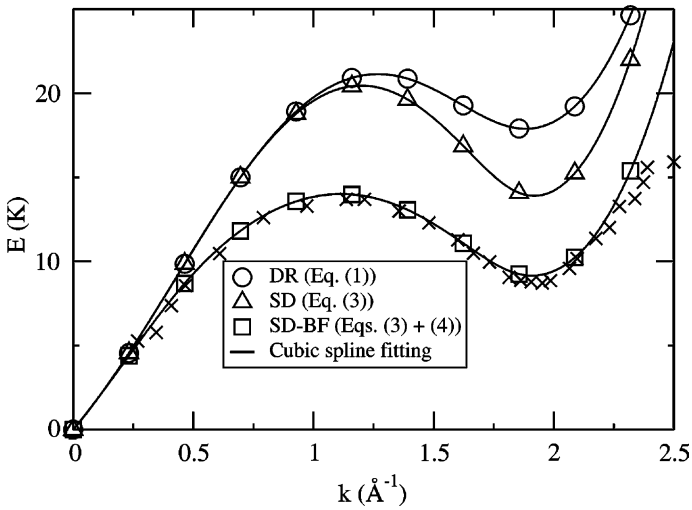

Fig. 5. Calculated dispersion relations for the following functionals: DR; Eq. (1), SD; Eq. (3), and SD–BF; Eqs. (3) and (4) are shown along with the experimental data [1–3].

momentum. Restrictions on the momenta k_i are introduced by the periodicity requirement of ψ. After this wavefunction has been propagated in real time (Eq. (11)) for sufficiently long period of time, which is dictated by the corresponding wave energies, the corresponding frequencies ω_i can be obtained by observing the period of liquid density oscillations ($N = 1$) or via 2-D space-time Fourier transform of ψ ($N \geqslant 1$). In the latter case it should be noted that the time axis is not periodic and therefore multiple cycles for frequencies should be recorded in order to minimize noise in the dispersion contour. Results for DR, SD, and SD–BF functionals along with reference data are shown in Fig. 5.

5. Stability tests and parallel scalability

Given the spatial step lengths ($\Delta x = \Delta y = \Delta z$) of the simulation cube and the time step Δt, it is now of interest to determine the relative accuracy of the method:

$$\mathrm{Err}(k) = \frac{|\omega_{k,\mathrm{calc}} - \omega_{k,\mathrm{exact}}|}{\omega_{k,\mathrm{exact}}} \times 100\%, \tag{21}$$

where k is the momentum of plane wave and ω correspond to the calculated and exact angular frequencies. In the following we have chosen waves from both phonon branch ($k = 0.5$ Å^{-1}) and close to the roton minimum ($k = 1.9$ Å^{-1}), where backflow is important. Result for the latter case is shown in Fig. 6, where nearly quadratic behavior with respect to the spatial step length is observed. The quadratic behavior for rotons is consistent with the accuracy of the applied finite differencing scheme. In general, the relative error for phonons appears to be an order of magnitude smaller than for rotons. Choice of time step appears to have only small effect on the accuracy of the method (in terms of Eq. (21)) but it strongly determines the overall stability of the method. If, for example, sub-nanosecond simulation length is desired then the time step should be chosen to be less than 80 fs. If too large time steps are combined with long simulation times then the amplitude of the excitation wave tends to grow significantly over time and the calculation will then yield unphysical results.

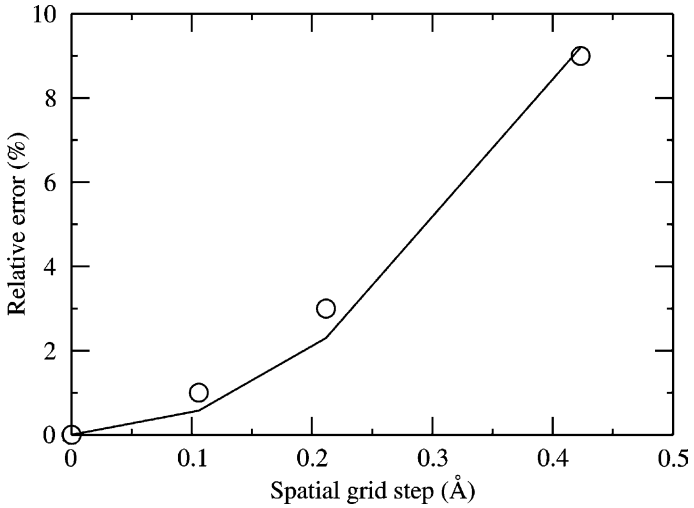

Fig. 6. Relative error in energy (Eq. (21)) for a plane wave with $k = 1.9$ Å^{-1} propagated with SD–BF (Eqs. (3) and (4)) is plotted as a function of spatial grid step length (circles) along with a quadratic function (continuous line). The following spatial step size and grid dimension combinations were used: 0.1 Å ($N = 256$), 0.2 Å ($N = 128$), and 0.4 Å ($N = 64$).

Efficient parallel execution was one of the primary goals when implementing the time integration method. In order to show the scalability properties approximately, we have chosen to measure the efficiency percentage obtained per one processor as a function of total number of processors (n) participating in the calculation:

$$\mathrm{Eff}(n) = \frac{T_1}{T_n \times n} \times 100\%, \tag{22}$$

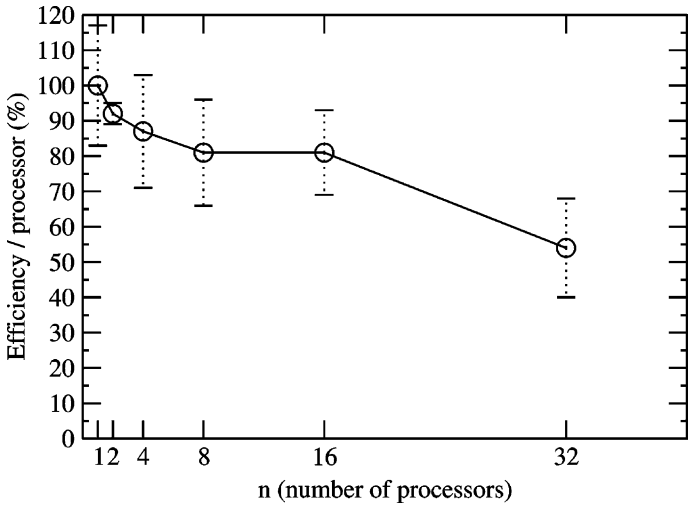

Fig. 7. Parallel scalability of the method is shown for SD–BF functional (Eqs. (3) and (4)) with a $256 \times 256 \times 256$ grid. Efficiency obtained per one processor (Eq. (22)) is plotted against the number of CPUs participating in the calculation. Error bars indicate the standard deviation in measured wall-clock times of different runs.

where T_n is the total wall-clock time for one time step (excluding initialization phase) in the calculation using n processors. Results of the parallel scalability runs are shown in Fig. 7 as a function of total number of processors. Error bars in the graph indicate variation of the measured wall-clock time within different runs. The reason for these time variations is that the computer used in the simulations was part of an active cluster of computers with random workloads. For large grid sizes ($N \sim 256$) the method scales very well up to $n = 16$ with efficiency per processor ca. 80%.

6. Conclusions

The presented numerical method can be used in modeling both static and dynamic phenomena in superfluid helium. Due to favorable numerical behavior of the scheme, even long-time scale dynamics can now be simulated without any geometry restrictions. However, memory requirements for storing the full 3-D spatial grid grow rapidly as the simulation cube is extended. With this respect the main restriction of the present approach is that it relies heavily on evenly spaced spatial grid. For this reason, it is not possible, for example, to simulate dynamics that involves long wavelength phonons in order of hundreds of Å. In such cases the feasible ways to perform calculations are to exploit high symmetry (e.g. [13]), to use non-uniform (adaptive) spatial grid, or to develop properly matched absorbing boundary conditions that can even cope with the long wavelength phonons.

Acknowledgements

Research funding by graduate school LASKEMO and computational resources by Center for Scientific Computing (CSC) are acknowledged. We also thank Dr. V.A. Apkarian and Dr. J. Toivanen for helpful discussions.

References

[1] H. Palvesky, K. Otnes, K.E. Larsson, Excitation of rotons in helium II by cold neutrons, Phys. Rev. 112 (1958) 11.
[2] D.G. Henshaw, Energy–momentum relation in liquid helium by inelastic scattering of neutrons, Phys. Rev. Lett. 1 (1958) 127.
[3] J.L. Yarnell, G.P. Arnold, P.J. Bendt, E.C. Kerr, Excitations in liquid helium: neutron scattering measurements, Phys. Rev. 113 (1959) 1379.
[4] R.P. Feynman, M. Cohen, Energy spectrum of the excitations in liquid helium, Phys. Rev. 102 (1956) 1189.
[5] E.P. Gross, Structure of quantized vortex, Nuovo Cimento 20 (1961) 454.
[6] E.P. Gross, Hydrodynamics of a superfluid condensate, J. Math. Phys. 4 (1963) 195.
[7] L.P. Pitaevskii, Vortex lines in an imperfect bose gas, Sov. Phys. JETP 13 (1961) 451.
[8] E. Madelung, Quantum theory in hydrodynamic form, Z. Phys. 40 (1927) 322.
[9] J. Dupont-Roc, M. Himbert, N. Pavloff, J. Treiner, Inhomogeneous liquid helium-4: a density functional approach with a finite-range interaction, J. Low Temp. Phys. 81 (1990) 31.
[10] F. Dalfovo, A. Lastri, L. Pricaupenko, S. Stringari, J. Treiner, Structural and dynamical properties of superfluid helium: a density-functional approach, Phys. Rev. B 52 (1995) 1193, and references therein.
[11] N. Berloff, Nonlocal nonlinear Schrödinger equations as models of superfluidity, J. Low Temp. Phys. 116 (1999) 359.
[12] J. Eloranta, N. Schwentner, V.A. Apkarian, Structure and energetics of He_2^* bubble states in superfluid ^{4}He, J. Chem. Phys. 116 (2002) 4039, and references therein.
[13] J. Eloranta, V.A. Apkarian, A time dependent density functional treatment of superfluid dynamics: equilibration of the electron bubble in superfluid ^{4}He, J. Chem. Phys. 117 (2002) 10139.
[14] F. Ancilotto, F. Faccin, F. Toigo, Wetting transitions of ^{4}He on alkali-metal surfaces from density-functional calculations, Phys. Rev. B 62 (2000) 17035.
[15] M.A. Woof, G.W. Rayfield, Energy of negative ions in liquid helium by photoelectric injection, Phys. Rev. Lett. 15 (1965) 235.
[16] B.E. Springett, R.J. Donnelly, Pressure dependence of the radius of the negative ion in helium II, Phys. Rev. Lett. 17 (1966) 364.

[17] J.A. Northby, T.M. Sanders Jr., Photoejection of electrons from bubble states in liquid helium, Phys. Rev. Lett. 18 (1967) 1184.
[18] C.C. Grimes, G. Adams, Infrared spectrum of the electron bubble in liquid helium, Phys. Rev. B 41 (1990) 6366.
[19] W.S. Dennis, E. Durbin Jr., W.A. Fitzsimmons, O. Heybey, G.K. Walters, Spectroscopic identification of excited atomic and molecular states in electron-bombarded liquid helium, Phys. Rev. Lett. 23 (1969) 1083.
[20] M. Stockton, J.W. Keto, W.A. Fitzsimmons, Ultraviolet emission spectrum of electron-bombarded superfluid helium, Phys. Rev. A 5 (1972) 372.
[21] J.W. Keto, F.J. Soley, M. Stockton, W.A. Fitzsimmons, Dynamic properties of neutral excitations produced in electron-bombarded superfluid helium. II. Afterglow fluorescence of excited helium molecules, Phys. Rev. A 10 (1974) 887.
[22] J.W. Keto, F.J. Soley, M. Stockton, W.A. Fitzsimmons, Dynamic properties of neutral excitations produced in electron-bombarded superfluid helium. I. The He (^{3}S) and He_2 ($a^3\Sigma_u^+$) atomic and molecular metastable states, Phys. Rev. A 10 (1974) 872.
[23] T. Kiljunen, L. Lehtovaara, H. Kunttu, J. Eloranta, Solvation of triplet Rydberg states of molecular hydrogen in superfluid helium (2003), unpublished.
[24] L. Giacomazzi, F. Toigo, F. Ancilotto, Dynamics of liquid ^{4}He in confined geometries from time-dependent density functional calculations (2003), unpublished.
[25] K.O. Keshishev, Yu.Z. Kovdrya, L.P. Mezhov-Deglin, A.I. Shalnikov, Mobility of charges in liquid helium up to its solidification, Sov. Phys. JETP 56 (1969) 94.
[26] A.V. Benderskii, J. Eloranta, R. Zadoyan, V.A. Apkarian, A direct interrogation of superfluidity on molecular scales, J. Chem. Phys. 117 (2002) 1201.
[27] N.G. Berloff, P.H. Roberts, Roton creation and vortex nucleation in superfluids, Phys. Lett. A 274 (2000) 69.
[28] M. Casas, F. Dalfovo, A. Lastri, L.L. Serra, S. Stringari, Density functional calculations of ^{4}He droplets, Z. Phys. D 35 (1995) 67.
[29] W.H. Press, S.A. Teukolsky, W.T. Vetterling, B.P. Flannery, Numerical Recipes in C: The Art of Scientific Computing, second ed., Cambridge University Press, Cambridge, UK, 1999.
[30] M. Frigo, S.G. Johnson, FFTW: an adaptive software architecture for the FFT, ICASSP Conf. Proc. 3 (1998) 1381. Available from http://www.fftw.org.
[31] T.E. Simons, P.S. Williams, On finite difference methods for the solution of the Schrödinger equation, Comput. Chem. 25 (1999) 513.
[32] OpenMP C and C++ application program interface. Available from http://www.openmp.org.
[33] M.A.L. Marques, A. Castro, G.F. Bertsch, A. Rubio, Octopus: a first-principles tool for excited electron-ion dynamics, Comp. Phys. Commun. 151 (2003) 60, See also. Available from <http://www.tddft.org/programs/octopus>.
[34] D.E. Woon, T.H. Dunning Jr., Gaussian basis sets for use in correlated molecular calculations. IV. Calculation of static electrical response properties, J. Chem. Phys. 100 (1994) 2975.
[35] T.H. Dunning Jr., Gaussian basis sets for use in correlated molecular calculations. I. The atoms boron through neon and hydrogen, J. Chem. Phys. 90 (1989) 1007.
[36] R.A. Kendall, T.H. Dunning Jr., R.J. Harrison, Electron affinities of the first-row atoms revisited. Systematic basis sets and wave functions, J. Chem. Phys. 96 (1992) 6796.
[37] Molpro is a package of ab initio programs written by H.-J. Werner and P.J. Knowles with contributions from R.D. Amos, A. Bernhardsson, A. Bering, et al., Theor. Chim. Acta 85 (1993) 423;
F. Eckert, P. Pulay, H.-J. Werner, J. Comput. Chem. 18 (1997) 1473.
[38] T. Kiljunen, J. Eloranta, J. Ahokas, H. Kunttu, Magnetic properties of atomic boron in rare gas matrices: an electron paramagnetic resonance study with ab initio and diatomics-in-molecules molecular dynamics analysis, J. Chem. Phys. 114 (2001) 7144.
[39] T. Kiljunen, J. Eloranta, J. Ahokas, H. Kunttu, Optical properties of atomic boron in rare gas matrices: an ultraviolet-absorption/laser induced fluorescence study with ab initio and diatomics-in-molecules molecular dynamics analysis, J. Chem. Phys. 114 (2001) 7157.
[40] M. Lax, The Franck–Condon principle and its application to crystals, J. Chem. Phys. 20 (1952) 1752.
[41] R. Kubo, Y. Toyozawa, Application of the method of generating function to radiative transitions of trapped electron in a crystal, Prog. Theor. Phys. 13 (1955) 160.
[42] P.W. Anderson, A method of synthesis of the statistical and impact theories of pressure broadening, Phys. Rev. 86 (1952) 809.